Radiation Heating Analysis

The Institute of Space and Astronautical Science
Report SP No. 17 March 2003

Development of a Radiation Analysis Code for Hypervelocity Reentry Applications

By

Kazuhisa FUJITA* and Takashi ABE*

(1 February 2003)

Abstract: The computer code SPRADIAN, a structured package for radiation analysis, has been developed. This study is primarily motivated by the MUSES-C sample return mission which encounters severe radiative environments during reentry into the earth atmosphere. In comparison with other radiation programs, much attention is paid to extension of the temperature range up to 100,000 K, detailed treatment of UV and VUV radiation, and flexibility with applications. The bound-bound, bound-free, and free-free transitions of monoatomic and diatomic species are taken into account. The emission and absorption coefficients of the bound-bound transition are calculated by the line-by-line method, while the others are computed by using corresponding cross-sections evaluated by the quantum defect method. In order to evaluate the radiative heating rate of the capsule, two approximate models are introduced to integrate the radiative heat transfer equation, in addition to a more detailed three-dimensional model. Accuracy of the program is examined, and some practical applications are reviewed.

1. INTRODUCTION

In the next century, human activities beyond the low earth orbit are expected to increase. Explorations into other planets of the solar system will be performed by entry probes, which may offer us much more information than obtained by remote-sensing. Space transportation between the ground and earth orbits will become more frequent, and its range will be extended when construction of space stations and lunar bases comes true. In order to realize such future missions, it is important to enhance our technology for safe return and recovery of reentry vehicles to the earth, and successful entry of probes into the atmospheric planets.

The Institute of Space and Astronautical Science is planning an asteroid sample return mission, namely the MUSES-C project for launch in 2002. In this mission, the return capsule is designed to reenter the earth atmosphere directly from an interplanetary orbit because of a severe restriction on satellite mass. Results of the primary studies (Suzuki et al. (1996), for example) predict that the maximum convective heat flux to the stagnation point amounts to more than 10 MW/m^2 at an altitude of 65 km and a velocity of 11.6 km/s, where the

* The Institute of Space and Astronautical Science, 3-1-1, Yoshinodai, Sagamihara, Kanagawa 229-8510, Japan.

temperatures in the nearly equilibrium region behind the shock wave become above 10,000 K, and the radiative heat flux to the stagnation point is expected to be more than 2 MW/m^2.

The convective heat flux is the major heating mechanism of atmospheric reentry vehicles when the reentry speed is below 8 km/s. However, the contribution of radiative heat flux becomes intensified with increasing the reentry velocity, and is not negligible any longer when the reentry velocity exceeds 10 km/s. In such a situation, line spectra and bound-free continua from atomic species become more significant than other radiation processes, and the ultra-violet (UV) and vacuum-ultra-violet (VUV) radiation should be treated more carefully. From a mission design standpoint, it is necessary to extend our knowledge about the radiation physics around the reentry vehicle to the extremely high-speed and high-temperature range, and to accurately estimate the radiative heat flux transferred to the surface of reentry vehicles. For extremely high-speed reentries, we can summarize the requirements for the radiation calculation code by

1) applicability to the temperature range up to 100,000 K.
2) applicability to a variety of gas species, air, ablation products, and extraterrestrial atmosphere, for example.
3) detailed treatment of emission and absorption in the UV and VUV range.
4) adaptability to application purposes and calculation cost.

There are several computer codes developed so far for radiation analysis (for example, see Park (1985), Whiting et al. (1996), and Hartung (1992)). However, some of them are classified, and others do not completely satisfy the requirements described above. For these reasons, we have newly developed a computer software package called SPRADIAN (the Structured Package for RADIation ANalysis), which consists of utility programs and a database for radiation analysis, using the latest spectroscopic constants and transition probabilities.

In this article, only brief outlines of the program package are shown, since detailed descriptions of the radiation physics incorporated in the computer programs are summarized in Fujita et al. (1997). In the following part of this article, Sec. 2 describes the radiative heat transfer models incorporated into SPRADIAN. In Sec. 3, the electronic transitions that are important in the radiative environments of atmospheric reentry vehicles are introduced. Finally, accuracy of the programs is discussed, and some practical applications are reviewed in Sec. 4.

2. RADIATIVE HEAT TRANSFER MODELS

2.1 Basic Formula

Radiation energy per unit solid angle passing normally through a unit area per unit time is called radiation intensity. In a gas medium in which emission and absorption occur simultaneously, a change of the radiation intensity in an arbitrary direction is described by the radiative transfer equation. Because, in general, emission and absorption intensities vary with the wavelength, the radiative transfer equation is given in terms of the emission and absorption coefficients at each wavelength :

$$\frac{dI}{dx} = \varepsilon - \kappa' I \tag{1}$$

where I [$Wm^{-2}sr^{-1}m^{-1}$] is the radiation intensity per unit wavelength, ε [$Wm^{-3}sr^{-1}m^{-1}$] is the emission coefficient per unit wavelength, κ' [m^{-1}] is the net absorption coefficient including

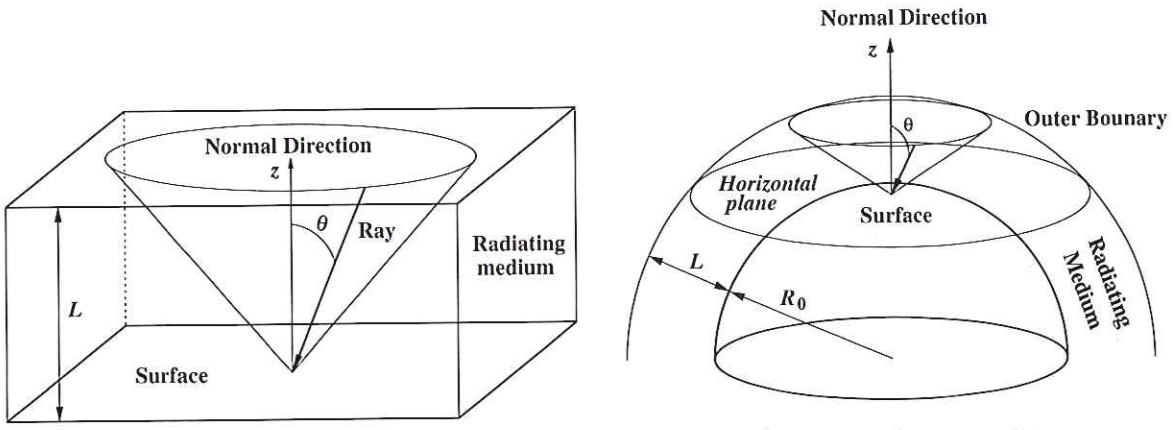

a) Tangent slab model b) Spherical cap model

Fig. 1: Geometry of 1-dimensional models.

induced emission, and x [m] is a coordinate aligned with the line of sight under consideration. SPRADIAN offers programs called `Self-abs` and `Ray-integ` to perform numerical integration of Eq. (1), for an isotropic and an anisotropic radiating medium, respectively, using a data set of ε and κ' prepared in the prescribed format. For more details, see Secs. 4.2 and 4.3 of Fujita, et al. (2000).

2.2 Tangent Slab Model

In general, the shock layer around the nose of reentry vehicles is axisymmetric about the stagnation point stream line, since the nose configuration is locally axisymmetric about this axis. At such a high reentry velocity as the radiative heat flux to the stagnation point is significant, the shock stand-off distance is small compared with the nose radius of vehicles, and a spatial change of physical properties is much severer in the direction normal to the shock than in the tangential direction. In such a situation, one-dimensional approximation of the shock layer yields a realistic estimation of the radiative heat flux transferred to the body surface.

Figure 2 1a) shows the geometry of the tangent slab model applied to the shock layer. In this approximation, local curvature of the shock layer is assumed to be negligibly small in comparison with thickness of the shock layer, and the z coordinate is aligned with the direction normal to the body surface. Physical properties are assumed to change only in the z direction, and to be uniform in the normal direction. Thus, all the physical properties in the shock layer are substituted with those along the stagnation point stream line (z coordinate) of the vehicle.

In this approximation, the radiative heat flux per unit wavelength transferred to a unit area of the surface, q [$\mathrm{Wm^{-2}m^{-1}}$], is given by (Sec.2.2 of Fujita, et al. (1997) Fujita, et al. (1997)).

$$q = 2\pi \int_0^{\pi/2} \sin\theta d\theta \int_0^L \varepsilon(z) \exp\left[-\frac{K(z)}{\cos\theta}\right] dz \tag{2}$$

where $K(z)$ is the optical depth in the z direction, defined by

$$K(z) \equiv \int_0^z \kappa'(z')dz' \tag{3}$$

The radiative heat flux can be calculated very quickly by the tangent slab model once $\varepsilon(z)$ and κ' are given. However, in reality, the radiative heat flux may be overestimated slightly by

this approximation, since the temperature behind the shock is the highest along the stagnation stream line, and since the local curvature of the shock layer is neglected. SPRADIAN offers a program called `1D-slab` to perform numerical integration of Eqs.(2) and (3), using a data set of ε and κ' defined along the z coordinate. For more details, see Sec. 4.4 of Fujita, et al. (2000).

2.3 Spherical Cap Model

A more realistic radiation analysis may be performed by using the spherical cap model, in which curvature of the shock layer and the body surface is taken into consideration. Figure 1 shows the geometry of this approximation. Concentric uniformity about the center of local curvature is assumed, so that this approximation is also of one-dimensional nature. The radiative heat flux to the surface is given by this approximation as (Sec.2.3 of Fujita, et al. (1997))

$$q = \pi \int_0^{\pi/2} \sin 2\theta d\theta \int_{R_0}^{R_0+L} \frac{\varepsilon(z) z dz}{\sqrt{z^2 - R_0^2 \sin^2\theta}} \exp\left[-\int_{R_0}^{R_0+z} \frac{\kappa'(z') z' dz'}{\sqrt{z'^2 - R_0^2 \sin^2\theta}} \right] \tag{4}$$

SPRADIAN offers a program called `S-cap` to perform numerical integration of Eq.(4), using a data set of ε and κ' defined along the z coordinate. For more details, see Sec. 4.4 of Fujita, et al. (2000).

A partial differential of q with respect to θ is called the angular radiation density function. It represents the radiation power transferred from the direction of θ. Let us consider a homogeneous shock layer as a special case, where $\varepsilon(z) = \varepsilon$ and $\kappa'(z) = \kappa'$. The angular radiation density is analytically obtained as

$$\rho(\theta; t) = \pi \frac{\varepsilon}{\kappa'} \sin 2\theta \left\{ 1 - \exp\left[-\frac{\kappa' L}{t} \left(\sqrt{\cos^2\theta + 2t + t^2} - \cos\theta \right) \right] \right\} \tag{5}$$

where $t \equiv L/R_0$ is the ratio of the shock stand-off distance to the nose radius of the vehicle. At the limit of $t \to 0$, which is the case of the tangent slab model, Eq.(5) becomes

$$\rho(\theta) = \pi \frac{\varepsilon}{\kappa'} \sin 2\theta \left[1 - \exp\left(-\frac{\kappa' L}{\cos\theta} \right) \right] \tag{6}$$

The angular radiation density is plotted for several values of t and $\kappa' L$ in Fig. 2. For $\kappa' L \geq 1$, the results of the spherical cap model are close to that of the tangent slab model ($t = 0$). On the other hand, the angular radiation density is more sensitive to the integration model when $\kappa' L \ll 1$. In general, $\kappa' L \gg 1$ is satisfied for the rays contributing to the major portion of radiative heat flux, because such rays are distributed among the short wavelength region with large absorption coefficients. In addition, t is generally much less than unity when the reentry velocity is extremely high. For these reasons, the radiative heat flux at the stagnation point is almost independent of the integration model in high-speed reentries.

2.4 Three Dimensional Model

The spherical cap model is generally a good approximation to estimate the radiative heat flux at the stagnation point as far as $t \ll 1$ and $\kappa' L \ll 1$ are fulfilled. However, its accuracy is expected to decrease when the nose radius becomes small in comparison with the shock stand-off distance, as illustrated in Fig. 3a). In addition, the spherical cap model does not apply to

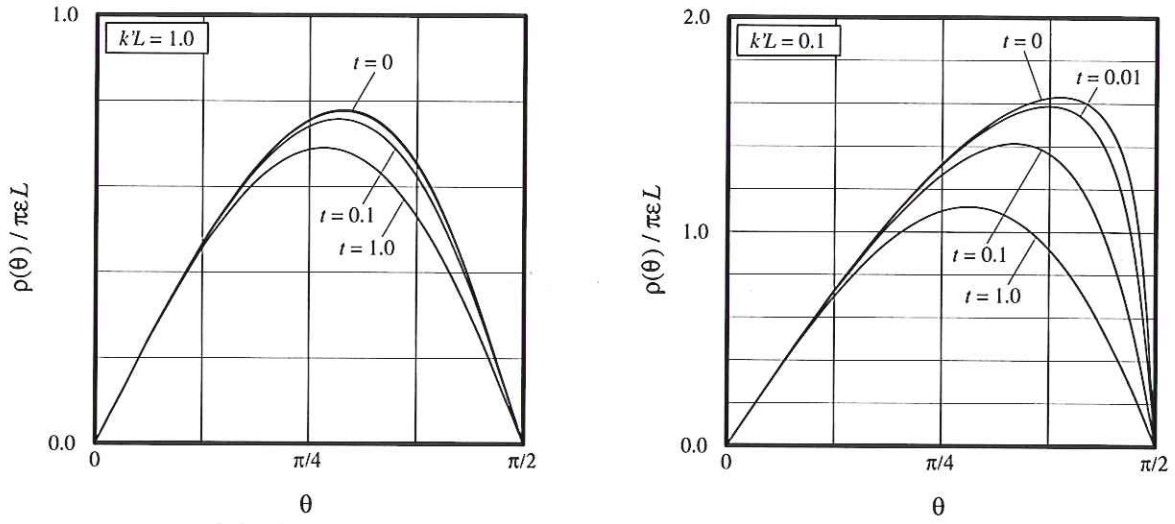

(a) $\kappa' L = 1.0$ (b) $\kappa' L = 0.1$

Fig. 2: Angular radiation density from a spherical homogeneous slab.

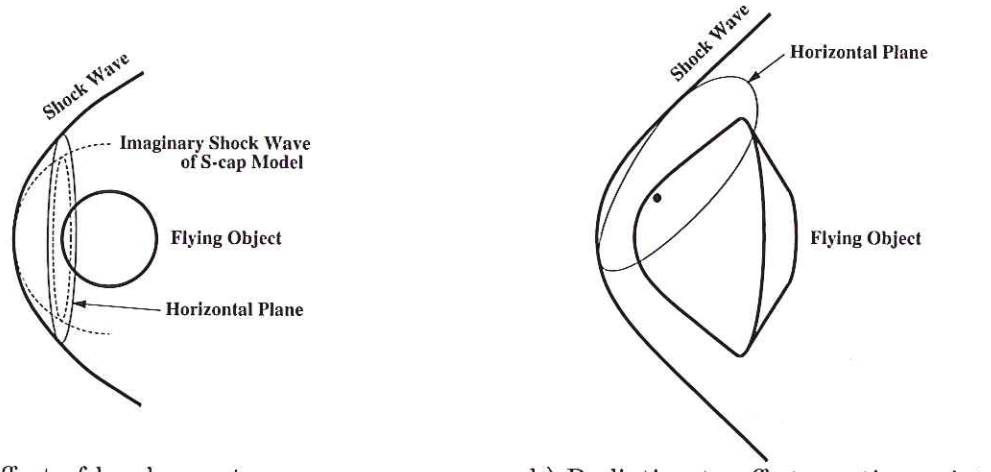

a) Effect of local curvature b) Radiation to off-stagnation point

Fig. 3: Deviation of spherical cap model.

calculate the radiative heat flux to the surface other than the stagnation point, as shown in Fig. 3b). In such cases, three dimensional numerical integration of the radiative heat transfer equation should be performed.

SPRADIAN offers a computer program called `3D-integ` to calculate the radiative heat flux transferred to an arbitrary location of the surface, using a data set of ε and κ' defined in the entire computation domain around the reentry vehicle. In `3D-integ`, the solid angle of 2π observable from the location on the surface under consideration is descretized into 324 solid-angle elements (36 azimuthal angles by 9 elevation angles), as illustrated in Fig. Fujita, et al. (2000). A local coordinate is set at the center of each solid-angle element, along which ε and κ' are recomputed and the radiative transfer equation is integrated toward the location on the surface. The total radiative heat flux transferred to this point is given by the sum of partial

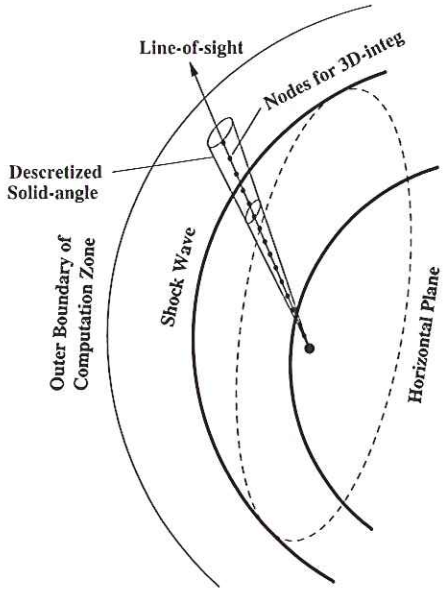

Fig. 4: Geometry of three dimensional radiative heat transfer model.

fluxes over 324 solid-angle elements. For more details, see Sec. 4.5 of Fujita, et al. (2000).

3. ELECTRONIC TRANSITIONS FOR REENTRY APPLICATIONS

When radiative heat flux transferred to reentry vehicles is significant, the major portion of radiative energy originates from electronic transitions of atoms and molecules. In SPRADIAN, the bound-bound, bound-free, and free-free electronic transitions of atomic species are taken into account as well as the electronic-vibrational-rotational transitions of diatomic species. Vibrational, rotational, and vibrational-rotational transitions of molecules are neglected since their contribution is negligibly small in high-temperature gases under consideration. Photo-dissociation, photo-ionization, and radiative recombination of molecular species are currently not taken into consideration. The electronic transitions incorporated into SPRADIAN version 1.5 PL4 are summarized in Table 1. Most important transitions that is considered to occur in high-temperature gas mixtures composed of hydrogen, helium, carbon, nitrogen, and oxygen are taken into consideration.

3.1 Bound-Bound Transitions

Emission and absorption in the bound-bound transition show characteristic line spectra since the discrete energy intervals are only permissible between the upper and lower levels. Radiation from high-temperature gases mainly results from the spontaneous and induced emission. The former is proportional to the number density of particles at the upper level, while the latter is proportional to radiation intensity in addition. The emission coefficient is, for this reason, defined in terms of the transition probability of spontaneous emission, i.e., the Einstein A coefficient, and the number density of particles at the upper level, as

$$\varepsilon(\lambda) = n_u \frac{hcA_{ul}}{4\pi\lambda_{ul}} \Phi(\lambda) \tag{7}$$

Table 1: Electronic transitions of atoms and molecules included in SPRADIAN version 1.5 PL4.

Transition type		Species		desig.	Index	Note
bound-bound (BB)	atomic line spectra	H		HI		215 lines
		He		HeI		324 lines
		C		CI		1286 lines
		N		NI		1091 lines
		O		OI		885 lines
		He^+		HeII		121 lines
		C^+		CII		651 lines
		N^+		NII		712 lines
		O^+		OII		857 lines
	molecular band spectra	H_2	$B^1\Sigma_u^+ \leftrightarrow X^1\Sigma_g^+$	H2	1	Lyman
			$C^1\Pi_u \leftrightarrow X^1\Sigma_g^+$		2	Werner
		N_2	$A^3\Sigma_u^+ \leftrightarrow X^1\Sigma_g^+$	N2	6	VK
			$B^3\Pi_g \leftrightarrow A^3\Sigma_u^+$		1	1+
			$C^3\Pi_u \leftrightarrow B^3\Pi_g$		2	2+
			$a^1\Pi_g \leftrightarrow X^1\Sigma_g^+$		5	LBH
			$b^1\Pi_u \leftrightarrow X^1\Sigma_g^+$		3	BH1
			$b'^1\Pi_u \leftrightarrow X^1\Sigma_g^+$		4	BH2
		N_2^+	$A^2\Pi_u \leftrightarrow X^2\Sigma_g^+$	N2+	2	Meinel
			$B^2\Sigma_u^+ \leftrightarrow X^2\Sigma_g^+$		1	1−
			$C^2\Sigma_u^+ \leftrightarrow X^2\Sigma_g^+$		3	2−
		O_2	$B^3\Sigma_u^- \leftrightarrow X^3\Sigma_u^-$	O2	1	SR
		NO	$A^2\Sigma^+ \leftrightarrow X^2\Pi_r$	NO	2	γ
			$B^2\Pi_r \leftrightarrow X^2\Pi_r$		1	β
			$C^2\Pi_r \leftrightarrow X^2\Pi_r$		3	δ
			$D^2\Sigma^+ \leftrightarrow X^2\Pi_r$		4	ε
		C_2	$A^1\Pi_u \leftrightarrow X^1\Sigma_g^+$	C2	2	Phillips
			$C^1\Pi_g \leftrightarrow A^1\Pi_u$		7	DA
			$D^1\Sigma_u^+ \leftrightarrow X^1\Sigma_g^+$		6	Mulliken
			$E^1\Sigma_g^+ \leftrightarrow A^1\Pi_u$		4	Freymark
			$b^3\Sigma_g^- \leftrightarrow a^3\Pi_u$		3	BR
			$d^3\Pi_g \leftrightarrow a^3\Pi_u$		1	Swan
			$e^3\Pi_g \leftrightarrow a^3\Pi_u$		5	FH
		CN	$A^2\Pi_i \leftrightarrow X^2\Sigma^+$	CN	2	Red
			$B^2\Sigma^+ \leftrightarrow X^2\Sigma^+$		1	Violet
		CO	$A^1\Pi \leftrightarrow X^1\Sigma^+$	CO	1	4+
			$B^1\Sigma^+ \leftrightarrow A^1\Pi$		2	Angstrom

Table 1: *Continued.*

Transition type		Species	desig.	Index	Note
bound-free (FB, BF)	continua	$H^+ + e \leftrightarrow H + h\nu$ $He^+ + e \leftrightarrow He + h\nu$ $C^+ + e \leftrightarrow C + h\nu$ $N^+ + e \leftrightarrow N + h\nu$ $O^+ + e \leftrightarrow O + h\nu$ $O + e \rightarrow O^- + h\nu$	HII/HI HeII/HeI CII/CI NII/NI OII/OI OI		
free-free (FF)	continua	N_2, N, O, N_2^+, O_2^+, NO^+, CO^+, H^+, He^+, C^+, N^+, O^+			Species are substituted with the ones accelerating electrons effectively.

where n [m^{-3}] is the number density, λ [m] is the wavelength, $\Phi(\lambda)$ [m^{-1}] is the line shape function to take account of the line broadening, and subscripts l and u represent the lower and upper levels, respectively. Contribution of the induced emission is incorporated into the net absorption, because both the induced emission and absorption occur simultaneously in proportion to the incident radiation intensity. Thus, the net absorption coefficient is given by

$$\kappa'(\lambda) = n_l \frac{A_{ul}\lambda_{ul}^4}{8\pi c}\frac{g_u}{g_l}\left(1 - R_{bb}\right)\Phi(\lambda) \tag{8}$$

where g is the statistical weight, and R_{bb} is the reduction factor of bound-bound transition defined by $R_{bb} = n_u g_l / n_l g_u$.

3.2 Bound-Free Transitions

The bound-free electronic transition involves absorption and emission of an electron :

$$A_l^{z-1} + h\nu \rightleftharpoons A_u^z + e \tag{9}$$

Since an electron is not bound in the upper state, emission and absorption due to the bound-free electronic transition show continuous spectra. The absorption coefficient of the bound-free transition, including the contribution of induced emission, is given by

$$\kappa'_{lu}(\lambda) = n_l \sigma_{lu}(\lambda)\left(1 - R_{bf}\right) \tag{10}$$

where $\sigma_{lu}(\lambda)$ is the cross section of the forward reaction (photo-absorption or photo-ionization cross section), and R_{bf} is the reduction factor of the bound-free transition. In SPRADIAN, free electrons participating in the bound-free and free-free transitions are assumed to have the Maxwell-Boltzmann velocity distribution. With this assumption, R_{bf} is defined by

$$R_{bf} = \frac{n_e n_u}{n_l}\frac{g_l}{2g_u}\left(\frac{h^2}{2\pi m_e k T_{el}}\right)^{\frac{3}{2}} \exp\left(-\frac{hc/\lambda - I_{ul}}{kT_{el}}\right) \tag{11}$$

where I_{ul} is the ionization energy of the lower state, n_e is the electron number density, T_{el} is the electron temperature, and m_e is mass of an electron. On the other hand, the emission coefficient is given by

$$\varepsilon_{ul}(\lambda) = n_u n_e \frac{h^4 c^2}{(2\pi m_e k T_{el})^{3/2}} \frac{g_l}{g_u} \frac{\sigma_{lu}(\lambda)}{\lambda^5} \exp\left(-\frac{hc/\lambda - I_{ul}}{kT_{el}}\right) \tag{12}$$

The total emission and absorption coefficients are given by summation of the individual coefficients calculated for possible pairs of upper and lower states. Such pairs are chosen according to selection rules for allowed transitions between the upper and lower states. For more details, see Sec. 5.2 of Fujita, et al. (1997).

3.3 Free-Free Transitions

When we refer to the free-free transition, a free electron and a z-valent atom are regarded as a $(z-1)$-valent particle in which the outermost electron is excited to a continuous level beyond the ionization limit. Therefore, the free-free radiation from $(z-1)$-valent particles is identical with the bremsstrahlung in which electrons are accelerated by z-valent particles (see Note in Table 1). This reaction is described as

$$\mathrm{A}^z + e_l + h\nu \rightleftharpoons \mathrm{A}^z + e_u \tag{13}$$

Here e_l and e_u represent electrons having the lower and upper kinetic energy, respectively, the difference of which is equivalent to energy of an emitted or absorbed photon. Since electron energy in both states changes continuously, emission and absorption in the free-free transition show continuous spectra.

The absorption coefficient including the contribution of induced emission is given by

$$\kappa'(\lambda) = n_{\mathrm{A}} n_e \sigma_{ff}^{z-1}(\lambda, T_{el})\,(1 - R_{ff}) \tag{14}$$

where σ_{ff}^{z-1} is the free-free absorption cross-section of the $(z-1)$-valent particle, and R_{ff} is the reduction factor of the free-free transition defined by

$$R_{ff} = \exp\left(-\frac{hc/\lambda}{kT_{el}}\right) \tag{15}$$

The emission coefficient is obtained from the net absorption coefficient by using Kirchhoff's law, since the reaction (13) can be regarded to be in equilibrium when free electrons are in the Maxwell-Boltzmann velocity distribution. The result is

$$\varepsilon(\lambda) = \frac{2hc^2}{\lambda^5} n_{\mathrm{A}} n_e \sigma_{ff}^{z-1}(\lambda, T_{el})\, R_{ff} \tag{16}$$

3.4 Transition Probabilities and Absorption Cross Sections

Atomic energy levels and transition probabilities of the bound-bound transition are taken from Wiese, et al. (1996) and NIST (2002) for C, N, O, and their ions. The data for H are taken from Wiese, et al. (1996) and Moore (1971). The energy levels of He and He^+, and the transition probabilities of He are taken from NIST (2002). The transition probabilities of He^+ are computed by the author, using the hydrogenic oscillator strengths given in Table 3–4 of

Griem (1964). Energy levels and transition probabilities of molecular species are computed from the spectroscopic data and the electronic transition moment. Accuracy of the results are validated by a large number of data available in the literature. For detailed information, see Chaps. 4.2 and 4.3 of Fujita, et al. (1997). Photo-absorption cross sections of the bound-free and free-free transitions are calculated by the quantum defect method (QDM) as described in Chap. 5 of Fujita, et al. (1997) except for the photo-detachment cross sections of O^-, which is determined from the experimental data of Branscomb, et al. (1965) and theoretical results of Garrett, et al. (1967), et al. (1967).

3.5 Accuracy

Because the radiation physics taken into account in SPRADIAN is accepted widely and believed to be reliable, accuracy of the computed results may be subject to (1) a lack of the prominent molecular bands and atomic lines, (2) errors in the transition probability and cross sections, and (3) bugs in the numerical codes. In order to eliminate these factors, we have conducted the comparative calculations by using NEQAIR (Park (1985)), and by using a large number of numerical results available in the literature (for example, Whiting et al. (1996), and Hartung (1992)). Park (1987), Moreau et al. (1992), Laux et al. (1992), Laux et al. (1993), Whiting et al. (1996), and Hartung (1992). As one of the typical benchmark results, Fig. 5a) shows a spectrum calculated by SPRADIAN for a high-temperature air plasma in equilibrium. The experimental spectrum shown in Fig. 5 is a reproduction of Fig.5.7 in Kruger et al. (1993). In this computation, the thermochemical conditions and plasma geometry are set identical with the experiment. Compared both quantitatively and qualitatively, the calculated spectrum is found in excellent agreement with the experimental one.

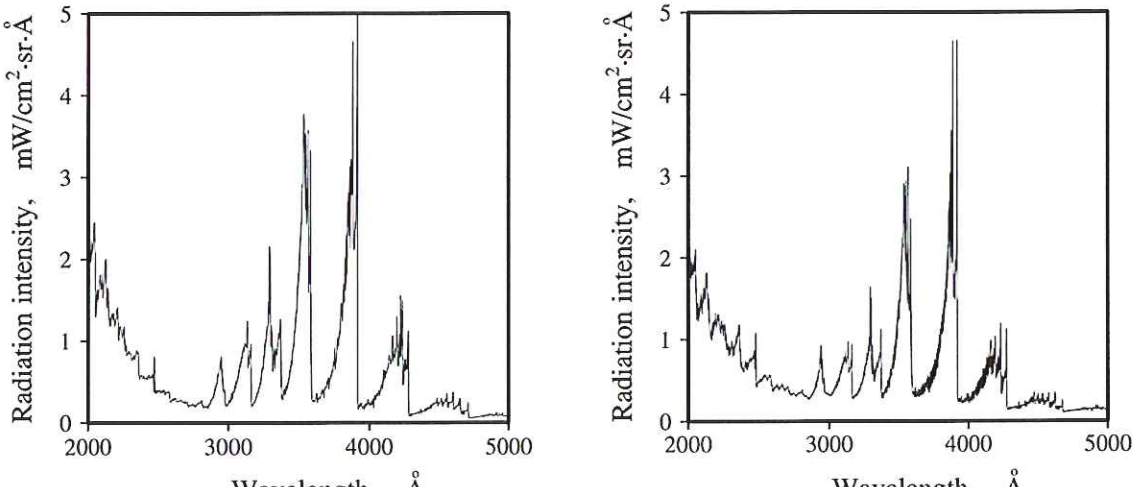

a) numerical (SPRADIAN) b) experimental (Kruger et al. (1993))

Fig. 5: Comparison of a spectrum calculated by SPRADIAN with experimental one.

4. TYPICAL APPLICATIONS

4.1 Measurement of Molecular Temperatures

Using SPRADIAN, molecular rotational and vibrational temperatures were measured behind a strong shock wave generated in a free-piston double-diaphragm shock tube (Fujita et al. (2002)). In this measurement, using nitrogen as the test gas, molecular spectra of N_2 (2+) and N_2^+ (1−) system were obtained behind the shock wave in the wavelength range of 270-520 nm by means of the repetitive time-frozen spectroscopy. Because of low spectral resolution in the experiment (typically 0.4 nm full-with at half maximum), a spectrum fitting technique was introduced to determine the rotational and vibrational temperatures from a composite spectrum of N_2 (2+) and N_2^+ (1−) system.

First, the spectra of N_2 (2+) and N_2^+ (1−) system were computed individually by SPRADIAN for the vibrational and rotational temperatures from 1,000 to 60,000 K at every 250 K interval. An observed spectrum were assumed to be a linear combination of N_2 (2+) and N_2^+ (1−) spectra, which could be reproduced from the numerical spectra of N_2 and N_2^+. Thus, the most appropriate pairs of numerical spectra were selected by minimizing the root-mean-square of the difference between the combined spectra and the observed one.

A typical numerical fit to the observed spectrum is presented in Fig. 6. The numerical spectrum is in good agreement with the measured spectrum for the range of $280 - 360$ nm. An increased deviation found in a longer wavelength region is accounted for by the contribution of atomic lines. In the case of Fig. 6, the rotational and the vibrational temperature of the N_2 C state are expected to be 4,500 and 5,500 K, respectively, while those of the N_2^+ B state are 21,000 and 9,000 K, respectively. This result suggests that the flow immediately behind the shock wave is in significant thermal nonequilibrium.

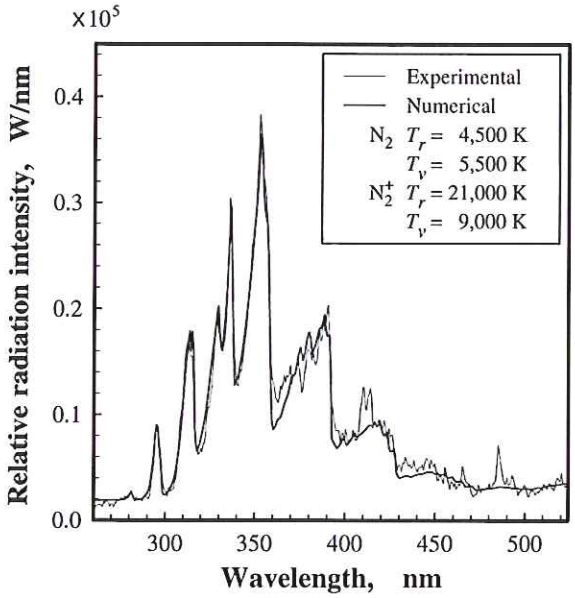

Fig. 6: Numerical fit to an observed spectrum at 2.6 mm behind the shock wave : test gas = N_2 ; pressure ahead of the shock = 0.3 torr ; shock velocity = 11.9 km/s (Fujita et al. (2002)).

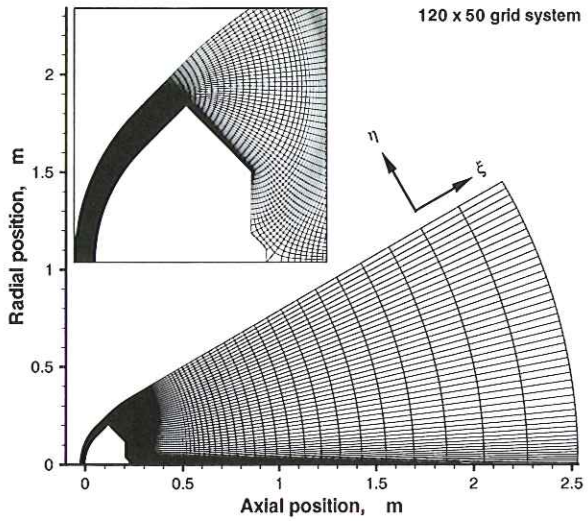

Fig. 7: A grid system used for CFD and radiation analysis of MUSES-C capsule (Fujita et al. (2003)).

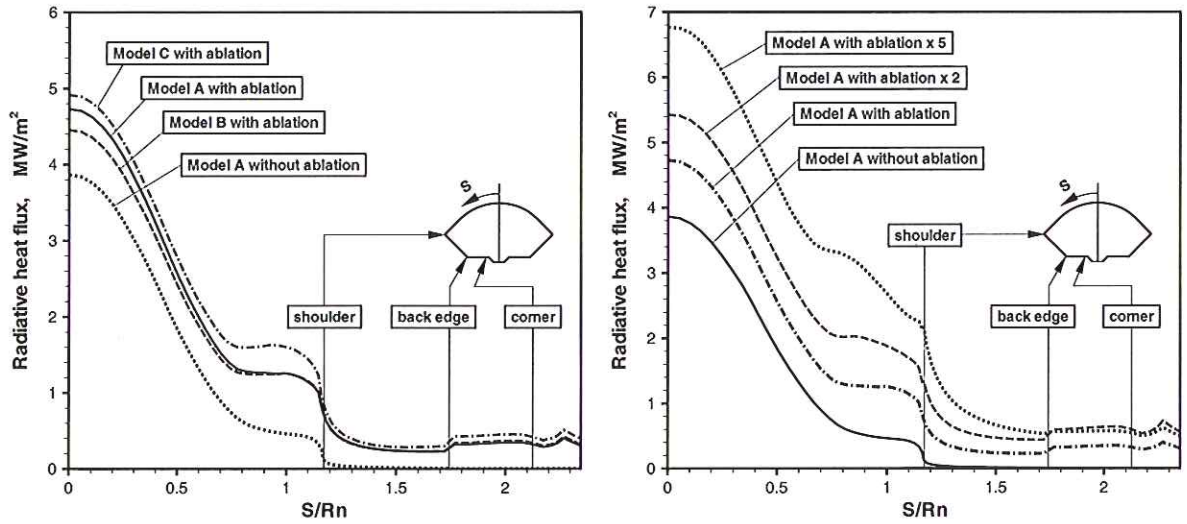

a) Effect of relaxation model b) Effect of ablation injection

Fig. 8: Radiative heat flux distributions around MUSES-C capsule : altitude = 56.2 km, velocity = 11.08 km/s (Fujita et al. (2003)).

4.2 Assessment of Radiative Heat Flux around MUSES-C Capsule

The radiative heat flux transferred to the MUSES-C reentry capsule was assessed by SPRADIAN (Fujita et al. (2003)). In this analysis, a hypersonic flow around the MUSES-C capsule was computed by a CFD code at first, using a grid system shown in Fig. 7. Thermal and chemical

Figure 8 shows the radiative heat flux distributions around the

nonequilibrium in the shock layer, and ablation of the heat shield material were taken into consideration. Using the flow result obtained above, the emission and absorption coefficients

of the high-temperature gas were calculated at each grid point by a program `CalSpec` included in SPRADIAN. Finally, the distribution of radiative heat flux around the capsule was obtained by solving the three-dimensional radiative heat transfer equation, using `3D-integ`, as described in Sec. 2.4.

capsule estimated at the altitude of 56.2 km, where the velocity and the Mach number of the capsule are expected to be 11.8 km/s and 34.1, respectively. In Fig. 8, S is the distance measured along the capsule surface from the stagnation point, and $R_n = 0.2065$ [m] is the nose radius. The curve denoted by Model B is the result of the nominal CFD model widely used. Model A represents the CFD model in which the thermochemical models are selected so that relaxation of the electronic and vibrational modes is faster than in Model B, and C is the one where the molecular internal modes of ablation products are frozen so that the electronic temperature is further overestimated than in Model A. In Fig. 8b), the injection rate of ablation products from the capsule surface is intentionally multiplied by 2 and 5.

The radiative heat flux around the capsule is found to depend considerably on the injection rate of ablation products, and less on the thermal models tested in this analysis. It should be noted that the radiative heat flux to the back body of the capsule is significantly underestimated unless the ablation processes are taken into consideration. The radiative heat flux increases with the injection rate of ablation products in two processes : an increase of the injection rate increases the shock stand-off distance, and an increase of ablation products in the shock layer, especially C and C_2, enhances the radiation in the shock layer, since such species are more apt to radiate than the atmospheric species even at low temperature.

5. SUMMARY

The structured package for radiation analysis, namely SPRADIAN, has been developed, and the theories incorporated in SPRADIAN are reviewed in this article. At present, SPRADIAN can be applied to 5 atomic species (H, He, C, N, O), 7 diatomic species (H_2, N_2, O_2, NO, C_2, CN, CO), their singly-ionized ions, and O^-. Utility programs included in SPRADIAN allows us to calculate the emission and absorption coefficients of high-temperature gas mixtures, regardless of thermal and chemical nonequilibrium, and to perform several types of radiative heat transfer calculations according to the purpose and the calculation cost. To demonstrate SPRADIAN, two typical applications conducted so far are reviewed at the end.

REFERENCES

Suzuki, K., Kubota, H., Fujita, K., and Abe, T., 1996, Numerical Analysis of Aerodynamic Heating on MUSES-C Reentry Capsule, ISTS 96-d-25, 20th International Symposium on Space Technology and Science.

Park, C., 1985, Nonequilibrium Air Radiation (NEQAIR) Program: User's Manual, NASA TM-86707.

Whiting, E.E., Park, C., Liu, Y., Arnold, J.O., and Paterson, A., 1996, NEQAIR96, Nonequilibrium and Equilibrium Radiative Transport and Spectra Program: User's Manual, NASA RP-1389.

Hartung, L.C., 1992, Development of a Nonequilibrium Radiative Heating Prediction Method for Coupled Flowfield Solutions, J. Thermophysics and Heat Transfer, **6**, pp. 618–625.

Fujita, K., and Abe, T., 1997, SPRADIAN, Structured Package for Radiation Analysis : Theory and Application, ISAS Report No. 669.

Fujita, K, 2000, SPRADIAN version 1.5 Users Manual, Manual version 2.3 (PL3), (in Japanese), http://kazuland.eng.isas.ac.jp/SPRADIAN.

Wiese, W.L., Fuhr, J.R., and Deters, T.M., 1996, Atomic Transition Probabilities of Carbon, Nitrogen, and Oxygen, A Critical Data Compilation, J. Phys. Chem. Ref. Data, Monograph **7**.

NIST Atomic Spectra Database, http://physics.nist.gov/cgi-bin/AtData/main_asd
Wiese, W.L., Smith, M.W., and Glennon, B.M., 1966, Atomic Transition Probabilities, Volume I Hydrogen Through Neon, NSRDS-NBS 4.
Moore, C.E., 1971, Atomic Energy Levels, Volume I Hydrogen Through Neon, NSRDS-NBS 35.
Griem, H.R., 1964, Plasma Spectroscopy, McGraw-Hill Book Company, New York.
Branscomb, L.M., Smith, S.J., and Tisone, G., 1965, Oxygen Metastable Atom Production Through Photodetachment, J. Chem. Phys., **43**, pp. 2906–2907.
Garrett, W.R., and Jackson Jr, H.T., 1967, Phys. Rev. **153**, pp. 28–35.
Park, C., 1987, Assessment of Two-Temperature Kinetic Model for Ionizing Air, AIAA Paper, AIAA 87-1574.
Moreau, S, Laux, C.O., Chapman, D.R., and MacCormack, R.W., 1992, A More Accurate Nonequilibrium Air Radiation Code: NEQAIR Second Generation, AIAA Paper, AIAA 92-2968.
Laux, C., Moreau, S., and Kruger, C., 1992, Experimental Study and Improved Modeling of High-Temperature Air Radiation, AIAA Paper, AIAA 92-2969.
Laux, C.O., Gessman, R.J., and Kruger, C.H., 1993, Modeling the UV and VUV Radiative Emission of High-Temperature Air, AIAA Paper, AIAA 93-2802.
Kruger, C.H. and Laux, C., 1993, Fundamental Processes in Partially Ionized Plasmas, AFOSR-TR-93-0007.
Fujita, K., Sato, S., Ebinuma, Y., and Abe, T., 2002, Experimental Investigation of Air Radiation from Behind a Strong Shock Wave J. Thermophysics and Heat Transfer, **16**, pp. 77–82.
Fujita, K., Otsu, H., Yamada, T., and Abe, T., 2003, Assessment of Hypersonic Reentry Environment around MUSES-C Capsule, Journal of the Japan Society for Aeronautical and Space Sciences (to be published).